

Article

The Effects of Si Substitution with C on the Amorphous Forming Ability, Thermal Stability, and Magnetic Properties of an FeSiBPC Amorphous Alloy

Wenzhong Zhu, Xiaoqian Jiang, Chen Chen, Shaojie Wu, Yongfu Cai, Fushan Li, Ran Wei ^{*}  and Tan Wang ^{*}

School of Materials Science and Engineering, Zhengzhou University, Zhengzhou 450001, China; zzu18239449456@gs.zzu.edu.cn (W.Z.); zzu18749202922@gs.zzu.edu.cn (X.J.); chenchenmse@zzu.edu.cn (C.C.); wushaojie@zzu.edu.cn (S.W.); yongfu_cai@zzu.edu.cn (Y.C.); fsliz@zzu.edu.cn (F.L.)

^{*} Correspondence: weiranmse@zzu.edu.cn (R.W.); wangtan@zzu.edu.cn (T.W.)

Abstract: The industrialization of Fe-based amorphous alloys with high a saturation magnetic flux density (B_s) has been limited so far due to their inadequate amorphous forming ability (AFA). In this study, the effects of substituting Si with C on the AFA, thermal stability, and magnetic properties of $\text{Fe}_{82}\text{Si}_{6-x}\text{B}_9\text{P}_3\text{C}_x$ ($x = 0-6$) alloys were systematically investigated. The experimental results demonstrate that the AFA, thermal stability, and soft magnetic properties can be significantly enhanced by the addition of C. Specifically, at a copper wheel velocity of 40 m/s, the $\text{Fe}_{82}\text{Si}_{6-x}\text{B}_9\text{P}_3\text{C}_x$ ($x = 2, 3, 4, 5$ and 6) alloy ribbons exhibit a fully amorphous structure in the as-spun state. The activation energy required for the α -Fe phase crystallization process in $\text{Fe}_{82}\text{Si}_{6-x}\text{B}_9\text{P}_3\text{C}_x$ ($x = 0, 2, 4$, and 6) alloys is determined to be 326.74, 390.69, 441.06, and 183.87 kJ/mol, respectively. Among all of the compositions studied, the $\text{Fe}_{82}\text{Si}_4\text{B}_9\text{P}_3\text{C}_2$ alloy exhibits optimized soft magnetic properties, including a low coercivity (H_c) of 1.7 A/m, a high effective permeability (μ_e) of 10608 ($f = 1$ kHz), and a relatively high B_s of 1.61 T. These improvements may be attributed to a more homogeneous and optimized magnetic domain structure being achieved through proper C addition. This work holds significant implications for the advancement of Fe-based soft magnetic amorphous alloys with high B_s .



Citation: Zhu, W.; Jiang, X.; Chen, C.; Wu, S.; Cai, Y.; Li, F.; Wei, R.; Wang, T. The Effects of Si Substitution with C on the Amorphous Forming Ability, Thermal Stability, and Magnetic Properties of an FeSiBPC Amorphous Alloy. *Metals* **2024**, *14*, 546. <https://doi.org/10.3390/met14050546>

Academic Editor: Jiro Kitagawa

Received: 30 March 2024

Revised: 26 April 2024

Accepted: 1 May 2024

Published: 4 May 2024



Copyright: © 2024 by the authors. Licensee MDPI, Basel, Switzerland. This article is an open access article distributed under the terms and conditions of the Creative Commons Attribution (CC BY) license (<https://creativecommons.org/licenses/by/4.0/>).

Keywords: Fe-based amorphous alloys; amorphous forming ability; soft magnetic properties; carbon addition

1. Introduction

The urgent need to address escalating environmental concerns and the energy crisis necessitates a reduction in the inefficient dissipation of energy. In order to power various applications, there is a growing interest in developing high-efficiency and high-performance devices like transformers and electric motors for electric vehicles. The efficiency of these devices greatly depends on the soft magnetic materials used within them [1–3]. Soft magnetic materials with desirable characteristics such as a high B_s , low H_c , and low core loss (P) can significantly enhance their efficiency. Consequently, extensive research has been conducted in recent years on Fe-based amorphous alloys, which exhibit low H_c and p values [4–6]. However, the currently widely used Metglas 2605SA1 (i.e., FeSiB series) has a lower B_s of 1.56 T compared to the 1.9–2.0 T of a silicon steel alloy, which hinders the miniaturization of soft magnetic devices [7]. Therefore, recent studies have primarily focused on enhancing the B_s properties of Fe-based amorphous alloys. For Fe-based amorphous alloys, the B_s value is primarily determined by the alloy's composition, indicating the magnetic moment per unit volume. Consequently, a higher percentage of Fe (wt.%) generally corresponds to a higher B_s [8]. Therefore, in recent years there has been an emphasis on increasing the Fe content (wt.%) in the design of high- B_s Fe-based amorphous alloys by considering metalloids with a lower relative atomic mass (B, C, Si and P) as the

primary alloying elements [9,10]. However, this conceptual approach results in a decrease in the AFA. When AFA approaches the glass formation limit, there is typically a tendency for partial hierarchical crystallization to occur on the surfaces of the as-cast ribbons during the melt-spinning process, while the majority of the ribbons still maintain an amorphous structure [11].

In 2006, Hitachi Metal successfully developed the FeSiBC series amorphous soft magnetic alloy [12], known as 2605HB1, and filed a patent application. This alloy exhibits a B_s greater than 1.6 T and an even lower H_c compared to the previously developed 2605SA1. However, due to its high iron content of approximately 80 at. %, the amorphous forming ability of alloy 2605HB1 is compromised. Chang [13] discovered that by combining Fe, B, P, C, and Si in the composition design process, a high B_s and AFA can be achieved. The addition of C optimizes the soft magnetic properties resulting in excellent characteristics for the $\text{Fe}_{83}\text{B}_{10}\text{C}_3\text{Si}_3\text{P}_1$ amorphous alloy with a high B_s value of 1.71 T and a low H_c value of 1.5 A/m [14]. It has been reported that adding small amounts of C into NANOMET alloys can enhance their AFA without compromising their soft magnetic properties [15,16]. The experimental results from Hui indicate that substituting C for Si significantly improves the AFA, B_s , and H_c of $\text{Fe}_{83.3}\text{Si}_{4-x}\text{B}_9\text{P}_3\text{Cu}_{0.7}\text{C}_x$ amorphous and nanocrystalline alloys [17]. However, it remains unclear how the C/Si ratio affects the structure and properties of Fe-based amorphous alloys or whether it can be further adjusted to enhance both their amorphous forming ability and soft magnetic properties.

In our current study, we have developed a novel $\text{Fe}_{82}\text{Si}_{6-x}\text{B}_9\text{P}_3\text{C}_x$ ($x = 0-6$) soft magnetic amorphous alloy system with a high iron content by substituting silicon with carbon. Systematic investigations on the AFA, magnetic properties, and magnetic domain structure were conducted. The underlying mechanism responsible for the enhanced AFA and optimized soft magnetic properties is thoroughly analyzed and discussed. These findings bear significant implications for the advancement of Fe-based soft magnetic amorphous alloys with high saturation magnetization.

2. Materials and Methods

The master alloy ingots were prepared by induction melting mixtures of high purity Fe (99.95 wt.%), Si (99.999 wt.%), C (99.99 wt.%), pre-alloyed Fe-B (B: 20 wt.%), and Fe-P (P: 18 wt.%) in a high-purity argon atmosphere with nominal compositions of $\text{Fe}_{82}\text{Si}_{6-x}\text{B}_9\text{P}_3\text{C}_x$ ($x = 0, 1, 2, 3, 4, 5$, and 6 in atomic percent). These alloys are denoted as C-0, C-1, C-2, C-3, C-4, C-5, and C-6 hereafter. These ingots were melted for over 5 min to ensure compositional homogeneity after complete melting. Ribbon specimens with a width of approximately 1 mm were prepared using a commonly employed single roller spinning machine under a high-purity argon atmosphere. The amorphous structure and thermal properties of the as-cast ribbons were investigated via X-ray diffraction (XRD) using Cu $K\alpha$ radiation and differential scanning calorimetry (DSC, NETZSCH 404, Selb, Germany) at a heating rate of 20 °C/min under Ar gas protection. For the isothermal annealing treatment, ribbon specimens were cut to approximately 70 mm in length, wrapped with aluminum foil, and then sealed in quartz tubes under vacuum conditions. Once the annealing furnace reached the desired temperature, the vacuum quartz tubes containing the ribbon specimens were placed into it and held for 10 min, followed by water quenching. The B_s were measured using a vibrating sample magnetometer (VSM, Lake Shore 7410, Columbus, OH, USA) under an applied field of 800 kA/m. The H_c and μ_e at 1 kHz were tested using a DC B-H hysteresis loop tracer (Linkjoin, MATS-2010SD, Loudi, Hunan, China) and an impedance analyzer (Agilent E4990 A, Santa Clara, CA, USA), respectively. The structure of the magnetic domain under different magnetic fields was characterized via magneto-optical Kerr microscopy.

3. Results and Discussion

3.1. Glass Forming Ability

To investigate the amorphous forming ability of the $\text{Fe}_{82}\text{Si}_{6-x}\text{B}_9\text{P}_3\text{C}_x$ ($x = 0, 1, 2, 3, 4, 5,$ and 6) alloy system, alloy ribbons were prepared using single roll spinning technology with copper wheel line velocities of 45 m/s and 40 m/s, respectively. The XRD patterns of the as-spun alloy ribbons are present in Figure 1. It can be observed from Figure 1a that at a velocity of 45 m/s, only a broad diffuse scattering peak around 44.5° is visible in the patterns, indicating the formation of an amorphous structure in the alloy ribbons. When the copper wheel velocity decreased to 40 m/s, in addition to the broad diffuse scattering peak at 44.5° , a sharp crystallization peak corresponding to the (200) plane of the α -Fe phase was observed in the region of $2\theta \sim 65^\circ$ for the C-0 alloy. For the C-1 alloy, there was a noticeable decrease in the intensity of this crystallization peak at 65° which suggests that partial crystallization occurred for both the C-0 and C-1 alloys in the as-spun state. However, for the C-2, C-3, C-4, C-5, and C-6 alloys, only a broad diffuse scattering peak appears in their respective XRD patterns, indicating that complete amorphous structures are achieved successfully within these five alloy ribbons.

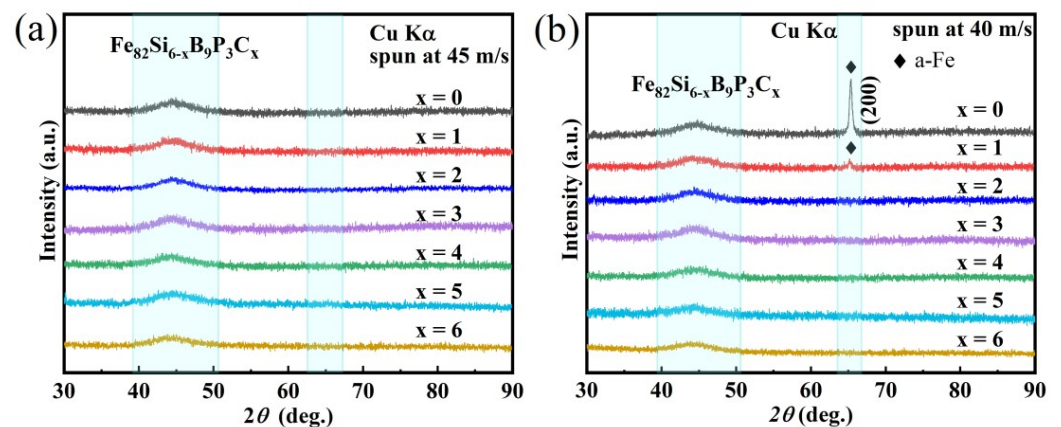


Figure 1. XRD patterns of the as-spun $\text{Fe}_{82}\text{Si}_{6-x}\text{B}_9\text{P}_3\text{C}_x$ alloy ribbons at different copper wheel line velocities: (a) 45 m/s; (b) 40 m/s.

Based on the XRD results presented above, it is suggested that the AFA of the $\text{Fe}_{82}\text{Si}_{6-x}\text{B}_9\text{P}_3\text{C}_x$ alloy can be enhanced efficiently through the substitution of Si with C. The improved AFA, resulting from the addition of the C element, can be attributed to factors such as atomic packing, thermodynamics principles, and empirical rules [18]. From a topological perspective, the atomic radii of iron, silicon, and carbon are 1.27 Å, 1.34 Å, and 0.86 Å, respectively. Substituting Si with C in the FeSiBPC alloy system leads to an increased difference in atomic sizes which becomes larger and more complex. This aligns with Inoue's rules which state that the difference between constituent elements' atomic sizes should exceed 12% for the formation of bulk metallic glasses. Additionally, the significant size difference among multiple components may result in highly packed atomic configurations within these alloys. Moreover, the presence of large negative mixing enthalpies among constituent elements contributes to high AFA levels. The substitution of Si with C increases the amount of negative mixing enthalpy due to a higher the Fe-C pairs having a higher value (-50 kJ/mol) compared to Fe-Si pairs (-35 kJ/mol) [19]. This enhancement positively impacts the AFA of these alloys.

Generally, the partial crystallization of an amorphous alloy primarily occurs on the free surface of alloy ribbons [20]. To further analyze the partial crystallization behavior of the C-0 and C-1 alloys under a velocity of 40 m/s, XRD tests were conducted on both the free surfaces and roller surfaces of the as-spun alloy ribbons. The results are presented in Figure 2a. The crystallization peak of (200) is exclusively observed on the free surface of the as-spun ribbons, while it is absent on the roller surface, indicating that crystallization

only occurs at the free surface due to its lower cooling rate. To further investigate the influences of cooling rate on the phase formation in the as-spun $\text{Fe}_{82}\text{Si}_{6-x}\text{B}_9\text{P}_3\text{C}_x$ alloy, C-0 and C-2 alloy ribbons were prepared with different cooling rates by adjusting the line velocity of the copper wheel. XRD analysis was conducted and the results are presented in Figure 2b,c. At a velocity of 30 m/s, a crystalline peak at 65° can still be observed on the free side of the C-0 alloy ribbon. For the C-2 alloy, despite a decrease in the velocity of the copper wheel from 40 m/s to 30 m/s, a fully amorphous structure is achieved in the as-spun ribbon, indicating the excellent AFA of the C-2 alloy. At lower speeds such as 20 m/s, 18 m/s, and 15 m/s, distinct differences are observed between the XRD patterns of the C-0 and C-2 alloys. On the free side, all ribbons exhibit prominent crystallization peaks at approximately 65° corresponding to the (200) plane of the α -Fe phase. On the roller side, a crystallization peak at 65° is observed for the C-2 alloy ribbons prepared at 15 m/s and 18 m/s, while no significant crystallization peak is observed at 20 m/s. For the C-0 alloy, only a small crystallization peak appears at around 65° in the XRD pattern of the ribbon prepared at 20 m/s. However, at both speeds of 15 m/s and 18 m/s, the C-0 alloy ribbons show multiple crystallization peaks near 44.5° , 65° , and 82.3° , corresponding to the (110), (200), and (211) planes of the α -Fe phase, respectively. Additionally, weak crystallization peaks related to the Fe(B, P) compound phase are also found at the left and right sides of 44.5° , indicating that the C-0 alloy ribbons prepared at 15 m/s and 18 m/s were highly crystallized. In summary, the higher the copper wheel velocity, the lower the intensity of the crystallization peak, and the more pronounced the amorphous broad diffuse scattering peak. Compared with the C-0 alloy, the C-2 alloy exhibits a lower degree of crystallization under the same fabrication conditions, which also suggests that the substitution of C for Si can improve the amorphous forming ability of the alloy system.

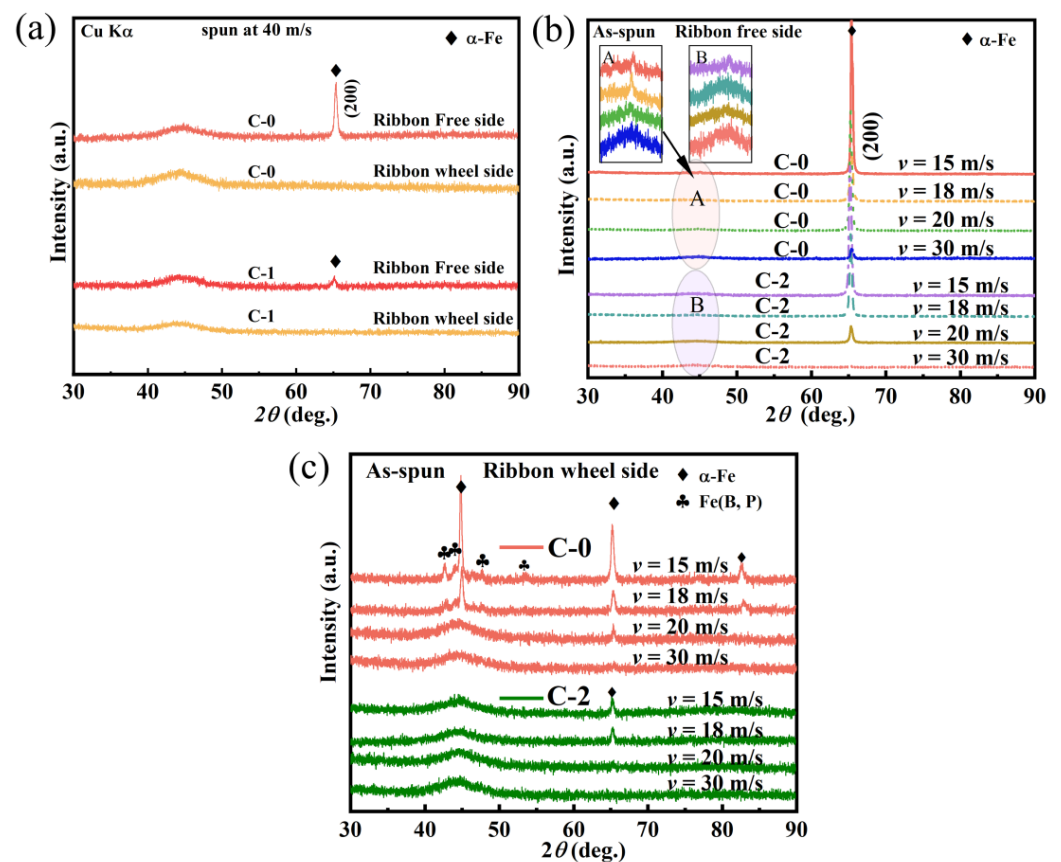


Figure 2. XRD patterns of as-spun C-0 and C-2 alloy ribbons prepared in different conditions. (a) C-0 and C-1 alloy ribbons prepared at 40 m/s; (b) XRD patterns of the free side of C-0 and C-2 alloy ribbons and (c) XRD patterns of the wheel side of C-0 and C-2 alloy ribbons.

The change in the thicknesses of the C-0 and C-2 alloy ribbons with the velocity of copper wheel is illustrated in Figure 3a. As depicted, an increase in velocity results in a decrease in ribbon thickness. Moreover, there is minimal variation observed between the thicknesses of the C-0 and C-2 alloy ribbons prepared under identical conditions. When considering a constant thermal conductivity for the copper wheel, a thinner alloy ribbon indicates a higher cooling rate, facilitating the formation of a fully amorphous structure. Notably, at a speed of 20 m/s, the thickness of the alloy ribbon is approximately twice that at 40 m/s; this discrepancy also accounts for the significant differences present in the XRD patterns at varying speeds. Additionally, as the alloy ribbon becomes thicker, there is an increased disparity in the cooling rates between the roller surface and the free surface, particularly evident at lower speeds, which further contributes to variations between their respective structures. Figure 3b summarizes the phase formation for both the C-0 and C-2 alloys across different cooling rates while comparing them to the $\text{Fe}_{83.3}\text{Si}_4\text{B}_8\text{P}_4\text{Cu}_{0.7}$ and $\text{Fe}_{84.75}\text{Si}_2\text{B}_9\text{P}_3\text{C}_{0.5}\text{Cu}_{0.75}$ alloys. The findings demonstrate that the C-2 alloy exhibits superior amorphous forming ability, which is conducive to its industrial production.

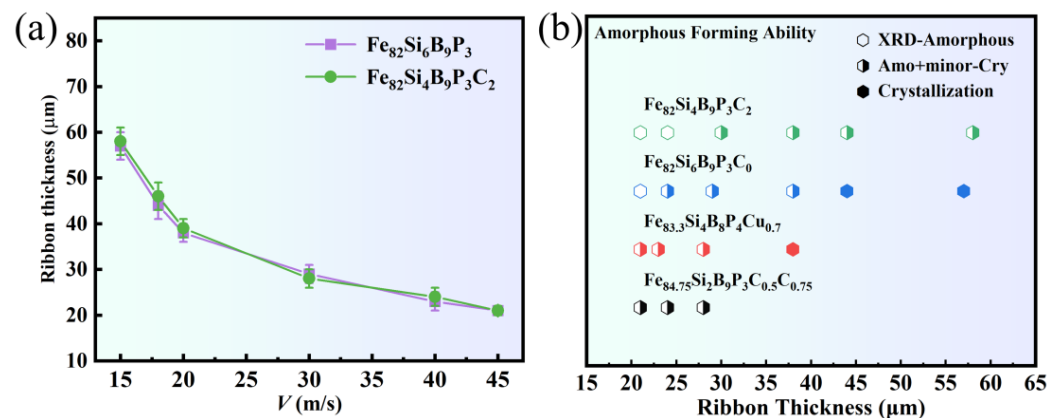


Figure 3. (a) The relationship between the thicknesses of C-0 and C-2 alloy ribbons and the line velocity of the copper wheel. (b) Schematic comparison of phase formation of different alloys under laboratory conditions and the RD patterns of as-spun C-0 and C-2 alloy ribbons prepared in different conditions.

3.2. Thermal Stability

The thermal stability of the as-spun $\text{Fe}_{82}\text{Si}_{6-x}\text{B}_9\text{P}_3\text{C}_x$ amorphous alloy ribbons was characterized through DSC analysis. To ensure a uniform comparison, all experimental samples were prepared as amorphous ribbons at a copper wheel velocity of 45 m/s. The DSC results are presented in Figure 4. All DSC curves exhibit two crystallization exothermic peaks, corresponding to the formation of a soft magnetic α -Fe phase and the precipitation of the Fe(B,P) compound phase, respectively. The results indicate that an increase in C content initially leads to an increase and then a decrease in the initial crystallization temperature (T_{x1}) of the α -Fe phase. Among these alloys, C-3 exhibits the highest T_{x1} value (491.4 °C). A higher T_{x1} suggests a greater difficulty in crystallization during the heating process, indicating an enhanced thermal stability. On the other hand, both the initial crystallization temperature (T_{x2}) and the peak temperature (T_{p2}) of the Fe(B,P) compound phase decrease with increasing C content; however, when the C content exceeds 2 at.% it becomes difficult to distinguish T_{x2} due to the presence of overlapping crystallization peaks. As shown in Figure 4b, all of the DSC curves display an endothermic peak corresponding to Curie temperature transition of amorphous alloys, with its peak representing the T_c point. It is observed that T_c initially increases and then decreases with increasing C content; among them, the C-3 alloy achieves the highest T_c value (368.3 °C). The TG analysis was conducted on the C-2 alloy ribbons to validate the accuracy of the T_c readings obtained from DSC.

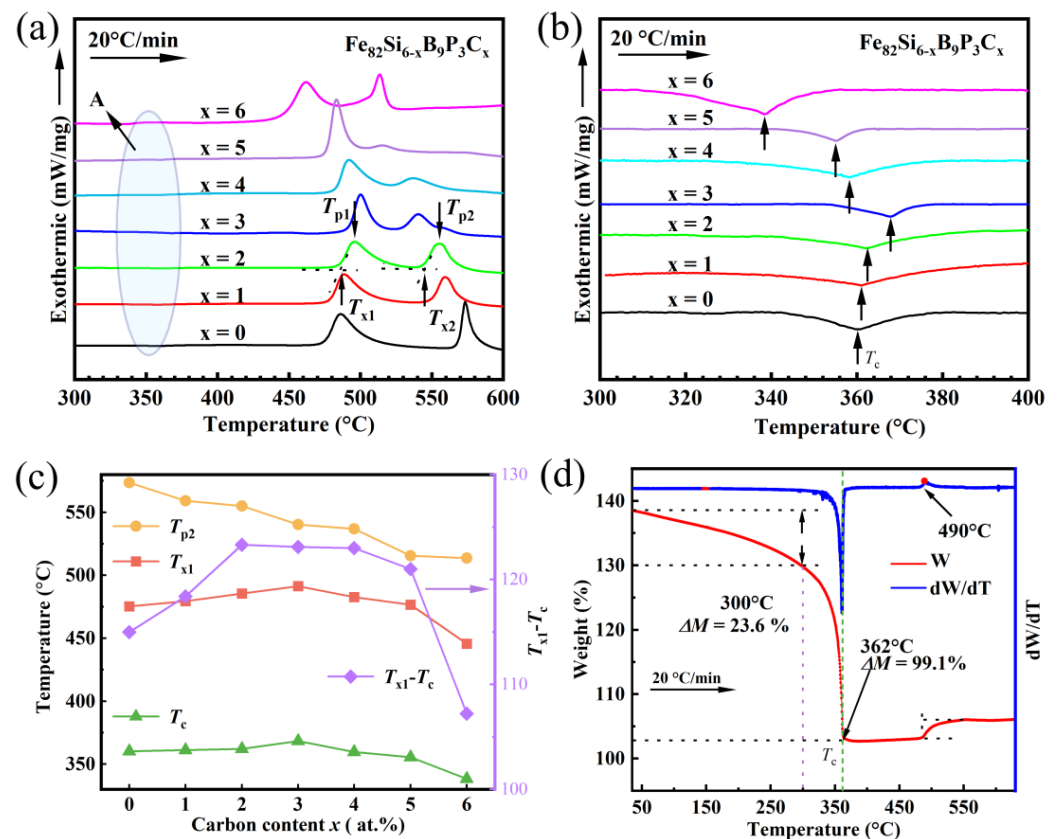


Figure 4. (a) DSC curves of as-spun Fe₈₂Si_{6-x}B₉P₃C_x amorphous alloys (x = 0–6) at a heating rate of 20 °C/min; (b) enlarged image of the A area in (a); (c) the changes in T_{x1}, T_{x2} and T_{x1}-T_c with C content; and (d) TG curve of C-2 alloy ribbons.

The excellent soft magnetic properties of most Fe-based amorphous alloys without Cu are attributed to the uniformity of their structure, and it is not anticipated that clusters or crystallization will occur during stress relief annealing [21]. T_{x1}-T_c is commonly employed as a quantitative measure for characterizing the ability of amorphous alloys to achieve favorable soft magnetic properties. A higher value indicates that the alloy can actuate stress-pinned magnetic domains more easily without undergoing crystallization during conventional annealing [22]. As shown in Figure 4c, the appropriate substitution of Si with C not only enhances the T_{x1} and T_c values of the alloy ribbon but also increases T_{x1}-T_c. The C-2, C-3, C-4, and C-5 alloys exhibit higher T_{x1}-T_c values, exceeding 120 °C, while the C-0, C-1, and C-6 alloys demonstrate lower T_{x1}-T_c values. When Si is replaced with C, both T_{x1} and T_c initially increase before decreasing. This phenomenon can be explained from two aspects: Firstly, taking into consideration the example of the C-0 alloy and C-2 alloy; after replacing Si with an appropriate amount of carbon (C) in a four-component Fe-Si-B-P-C system, it transforms into a five-component Fe-Si-B-P-C system which may have a microalloying effect resulting in a more complex configuration of the amorphous structure. Additionally, this atomic size difference enhances the thermal stability within the amorphous structure, resulting in a significant increase in T_{x1} from 475.3 °C to 485.5 °C, while T_c shows only marginal improvement due to short-range order effects within amorphous alloys (from 360.3 °C to 362.2 °C). Consequently, there is an overall increase in the value of T_{x1}-T_c. Secondly, taking into account examples such as the C-4 and C-6 alloys and following the excessive substitution of Si with C, the system transitions from a five-component Fe-Si-B-P-C system back to a four-component Fe-C-B-P system where any microalloying effects disappear potentially improving order degree within amorphous structures. Moreover, due to their larger size compared to C atoms, Si atoms have an increased propensity for impeding atomic diffusion motion. Consequently, a scarcity of Si atoms and an elevated

level of order in the amorphous structure result to a pronounced decrease in its thermal stability. Specifically, T_{x1} is significantly reduced from 482.7 °C to 445.8 °C, while T_c also experiences a reduction albeit within a narrower range than T_{x1} (from 123.0 °C to 107.4 °C). Therefore, $T_{x1}-T_c$ is also reduced.

The thermal stability and non-isothermal crystallization behavior of $\text{Fe}_{82}\text{Si}_{6-x}\text{B}_9\text{P}_3\text{C}_x$ amorphous alloy ribbons were further investigated by conducting DSC tests at different heating rates (10, 20, 30, and 40 K/min) for C-0, C-2, C-4, and C-6 alloys. The resulting DSC curves are presented in Figure 5. It is evident that as the heating rate increases from 10 °C/min to 40 °C/min, the crystallization peaks shift towards higher temperatures, indicating pronounced kinetic characteristics. This phenomenon can be attributed to the fact that at lower heating rates, atoms within the amorphous structure have sufficient time to absorb energy for motion and diffusion rearrangement leading to crystallization at lower temperatures. Conversely, higher heating rates result in shorter atomic diffusion and rearrangement times within the amorphous phase, thereby pushing the crystallization process towards higher temperatures [23,24].

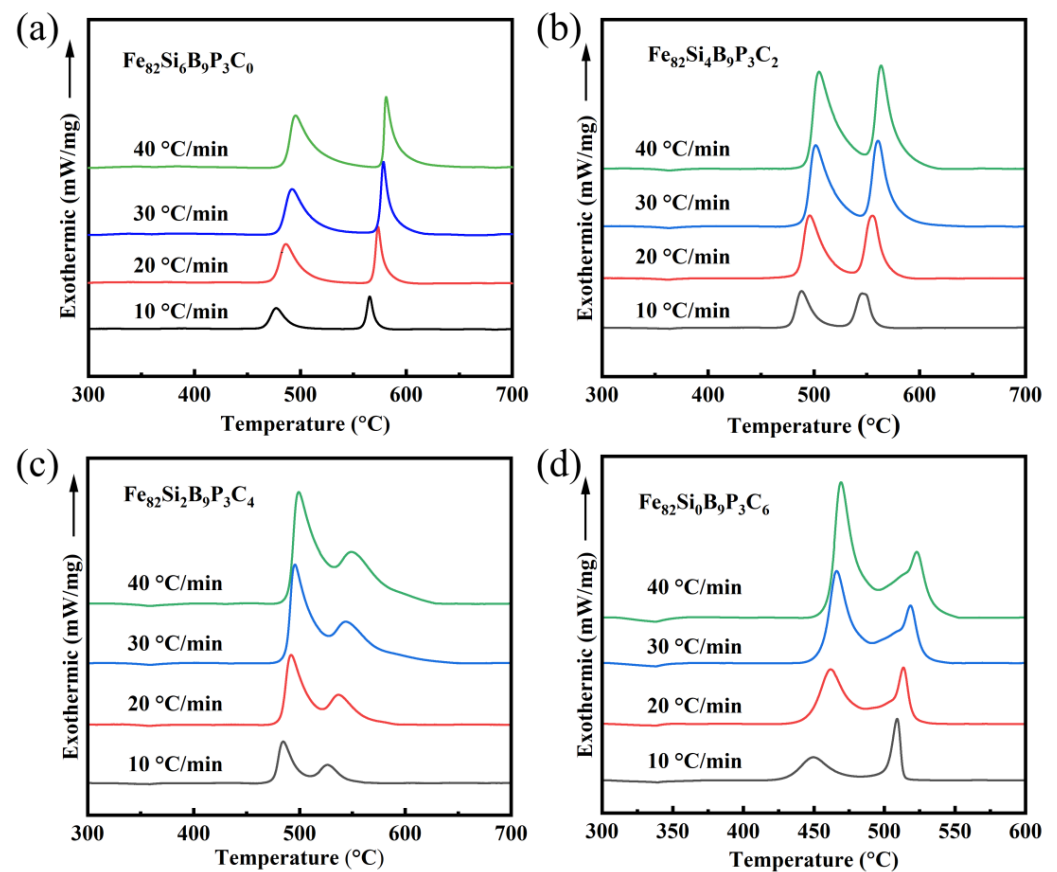


Figure 5. DSC curves of as-spun $\text{Fe}_{82}\text{Si}_{6-x}\text{B}_9\text{P}_3\text{C}_x$ amorphous alloys at heating rates of 10, 20, 30, and 40 K/min: (a) C-0 alloy, (b) C-2 alloy, (c) C-4 alloy, and (d) C-6 alloy.

In the process of crystallization, the amorphous structure must absorb sufficient energy to overcome a specific energy barrier known as the activation energy (E_a). A higher E_a indicates greater stability of the amorphous structure. Based on the characteristic temperature values obtained from DSC curves, the activation energies for α -Fe phase crystallization process in $\text{Fe}_{82}\text{Si}_{6-x}\text{B}_9\text{P}_3\text{C}_x$ amorphous alloys were determined using the Kissinger equation, as shown in Figure 6. The activation energies derived for the α -Fe phase crystallization process are presented in Table 1. It is observed that as the C content increases, E_{p1} and E_{x1} initially increase before decreasing again in the $\text{Fe}_{82}\text{Si}_{6-x}\text{B}_9\text{P}_3\text{C}_x$ alloy system. Among all four of the alloys, the C-4 alloy exhibits the highest E_{x1} of 441.06 kJ/mol and E_{p1}

of 465.09 kJ/mol, indicating that an appropriate substitution of C for Si element enhances thermal stability of the $\text{Fe}_{82}\text{Si}_{6-x}\text{B}_9\text{P}_3\text{C}_x$ amorphous alloys. However, when the carbon content continues to rise in the C-6 alloy, E_{x1} and E_{p1} decreases significantly. Notably, the E_{p1} values are slightly higher than the E_{x1} values for the C-0, C-2, C-4, and C-6 alloys, suggesting that grain growth in the α -Fe(Si) phase is more difficult than nucleation in this alloy system [25].

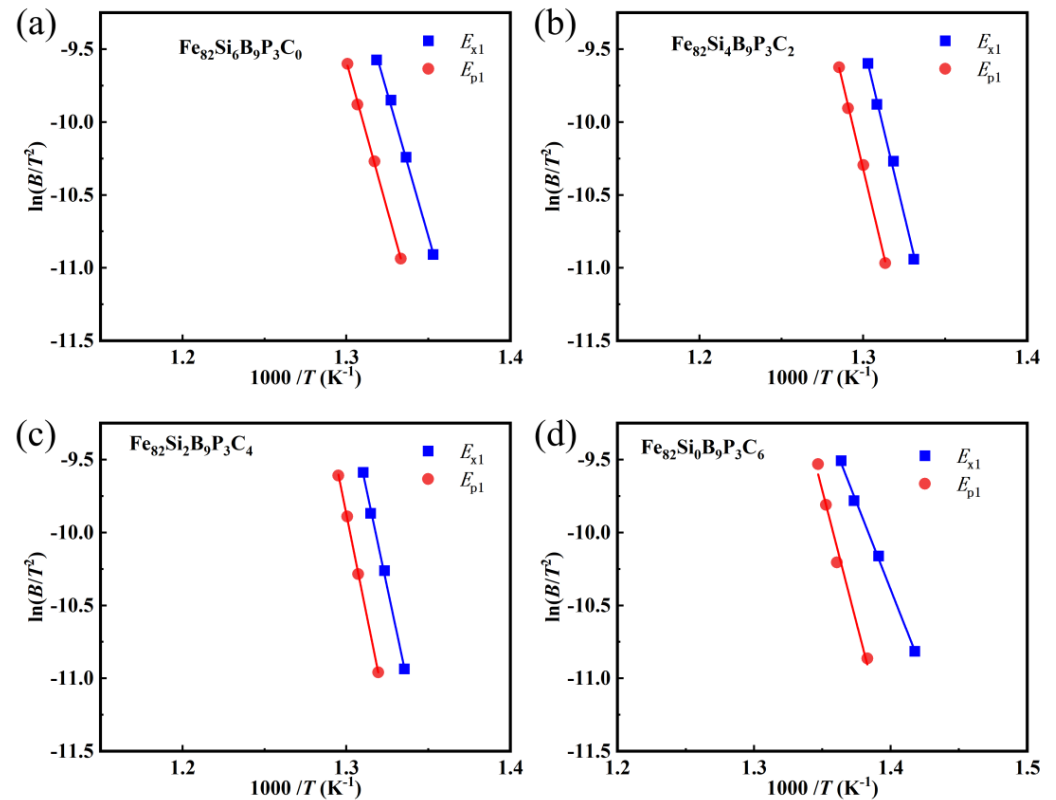


Figure 6. The Kissinger curves of $\ln(\beta/T^2)$ versus $(1/T)$ of as-spun $\text{Fe}_{82}\text{Si}_{6-x}\text{B}_9\text{P}_3\text{C}_x$ amorphous alloys: (a) C-0 alloy, (b) C-2 alloy, (c) C-4 alloy, and (d) C-6 alloy.

Table 1. The activation energies for the α -Fe phase crystallization process derived from the Kissinger curves.

Composition	E_{x1} (kJ/mol)	E_{p1} (kJ/mol)
$\text{Fe}_{82}\text{Si}_6\text{B}_9\text{P}_3$	326.74	338.88
$\text{Fe}_{82}\text{Si}_4\text{B}_9\text{P}_3\text{C}_2$	390.69	393.71
$\text{Fe}_{82}\text{Si}_2\text{B}_9\text{P}_3\text{C}_4$	441.06	465.09
$\text{Fe}_{82}\text{B}_9\text{P}_3\text{C}_6$	183.87	301.88

3.3. Magnetic Properties

For soft magnetic alloys, the values of H_c and μ_e are influenced by the structure, making the annealing treatment crucial in modulating these parameters. The H_c and μ_e of samples annealed at different temperatures are presented in Figure 7. As the annealing temperature increases, the H_c of all alloy ribbons initially decreases and then increases. From Figure 7a, it can be observed that the H_c of the alloy system decreases and reaches its minimum value when the annealing temperature rises to approximately 360–380 °C. Subsequently, as the temperature further increases towards T_{x1} , H_c starts to rise again. With an increase in C content, the H_c (i.e., lowest point on the curve) at the optimum annealing temperature first decreases and then increases. For the C-0, C-1, and C-6 alloys, the lowest point of H_c occurs at 360 °C, with corresponding values of 4.1, 3.8, and 4.8 A/m,

respectively. On the other hand, for the C-2, C-3, C-4, and C-5 alloys, the lowest point of H_c occurs at 380 °C. Among these alloys, the C-2 alloy exhibits the lowest H_c (1.7 A/m), the while C-3, C-4, and C-5 alloys have similar lowest H_c values (2.3, 2.2, and 2.8 A/m, respectively). The change in H_c with annealing temperature for these alloy ribbons can be understood based on the structural evolution that occurs during annealing. Currently, Fe-based amorphous ribbons are primarily produced using single roll melt spinning technology, which results in a high cooling rate and consequently generates significant internal stress within the as-spun ribbon [26]. Annealing prior to T_{x1} allows for the release of this internal stress induced by single roll melt spinning technology, leading to alterations in the microscopic stress field of atoms [27]. In this context, we propose that the decrease in H_c at 360–380 °C can be attributed to relaxation of the amorphous structure. Furthermore, as T_a approaches T_{x1} , the increase in H_c is associated with magnetoelastic anisotropy [28] coupled with magneto-crystalline anisotropy caused by the precipitation of α -Fe grains within the amorphous matrix. As shown in Figure 7b, μ_e shows an inverse relationship with annealing temperature compared to H_c . For the C-0, C-1, and C-6 alloys, the highest point of μ_e appears at 360 °C with corresponding values of 7800, 8134, and 7163, respectively. The C-2 alloy exhibits the highest μ_e value of 10,608, followed by 10,108 for C-3, 10,333 for C-4, and 7984 for the C-5 alloy. The magnetic susceptibility is determined at a low applied magnetic field by measuring the displacement of the domain walls, which can vary in width depending on the magnetic anisotropy. The enhancement of μ_e that occurred when the ribbons were annealed at the optimal temperature can be attributed to the decrease in magnetoelastic anisotropy caused by the release of internal stress. In summary, for $\text{Fe}_{82}\text{Si}_{6-x}\text{B}_9\text{P}_3\text{C}_x$ amorphous alloy ribbons, the substitution of Si elements with an appropriate C element can optimize the soft magnetic performance; however, the excessive replacement of the Si element with the C element may deteriorate the soft magnetic performance.

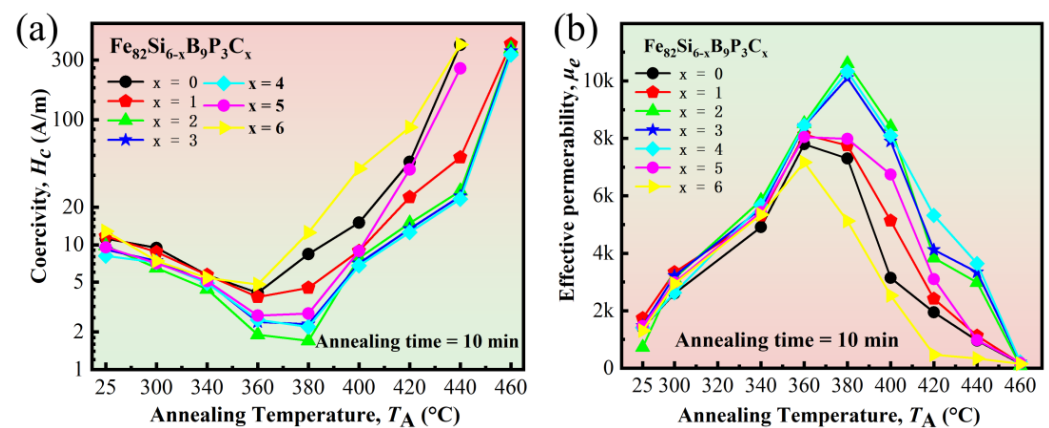


Figure 7. Annealing temperature (T_a) dependence of (a) H_c and (b) μ_e for $\text{Fe}_{82}\text{Si}_{6-x}\text{B}_9\text{P}_3\text{C}_x$ amorphous ribbons annealed for 10 min.

The variation in μ_e with frequency under different applied magnetic fields for C-0, C-2, C-4, and C-6 alloy ribbons annealed at the optimum temperature is shown in Figure 8, respectively. It can be observed that when the amplitude of the applied magnetic field remains constant, the μ_e of all alloy ribbons decreases as the frequency increases, which is a characteristic inherent to soft magnetic materials. As the frequency increases, the movement and rotation of magnetic moments within the domain walls and domains respond to the applied magnetic field. However, when they reach a certain frequency limit, their mobility becomes restricted and their contribution to magnetization rotation diminishes significantly, resulting in a sharp decline in μ_e [29]. Furthermore, it can be observed that, for frequencies below 20 kHz, μ_e gradually increases with increasing AC field amplitudes (H_m) for the C-0, C-2, C-4, and C-6 alloys until it reaches a specific value where further increase in H_m leads

to a decrease in μ_e . The AC field amplitude required for achieving maximum permeability can be considered as a pinning field (H_p) for these ribbons [30]. Figure 8 shows that the H_p values were determined as follows: 25 A/m for the C-0 alloy; 15 A/m for the C-2 alloy; 20 A/m for the C-4 alloy; and 30 A/m for the C-6 alloy, respectively. A lower H_p indicates fewer pinned sites, fewer defects, and better magnetic softness.

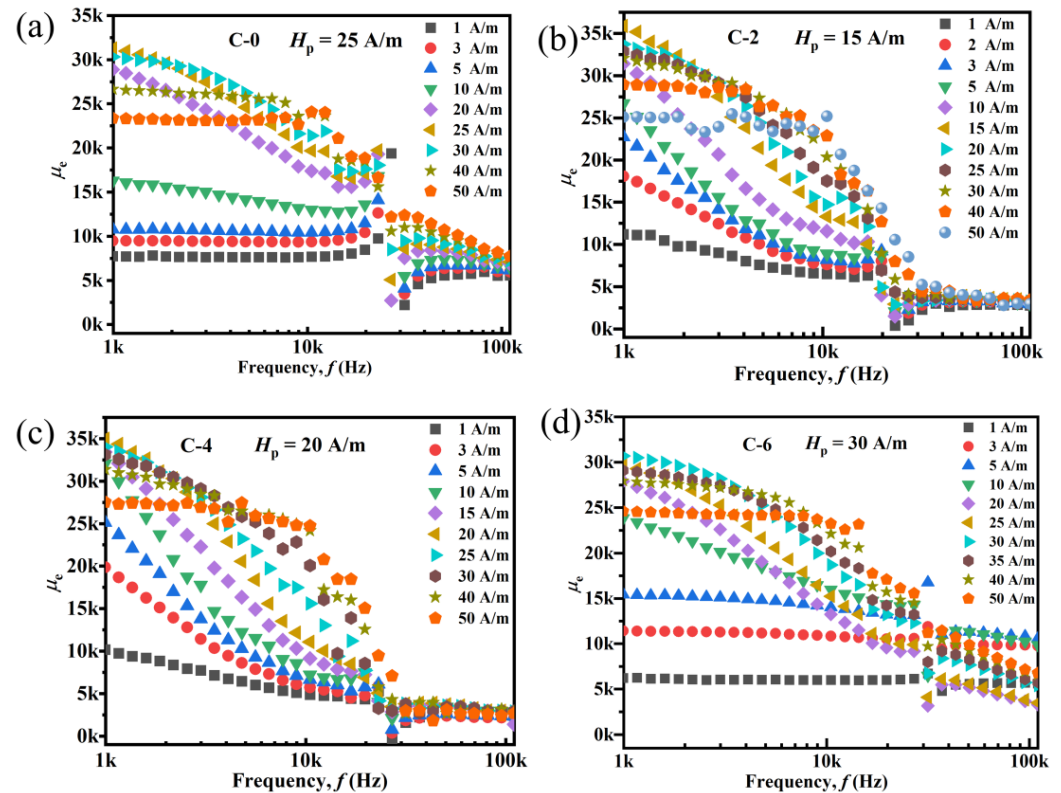


Figure 8. The variations of μ_e with f for annealed ribbons under different H conditions: (a) C-0 alloy, (b) C-2 alloy, (c) C-4 alloy, and (d) C-6 alloy.

The B_s parameter of the alloy is a crucial magnetic property, and VSM tests were conducted on the ribbons annealed at the optimal annealing temperature. The resulting Hysteresis loops are presented in Figure 9. To further investigate the influence of C addition on the soft magnetic properties of $\text{Fe}_{82}\text{Si}_{6-x}\text{B}_9\text{P}_3\text{C}_x$, the relationship between H_c , μ_e , and B_s with varying C content is summarized in Table 2. As depicted in Figure 9, all of the amorphous alloy samples exhibit rapid saturation magnetization under a small applied magnetic field, indicating the presence of typical soft magnetic characteristics within this alloy system. With the inclusion of C, it becomes evident from Table 2 that the values of B_s significantly increase from 1.59 T for the C-0 alloy to 1.63 T for the C-6 alloy. The enhancement in B_s can be explained from two perspectives: Firstly, since C has a smaller relative atomic mass than Si, replacing Si with C in $\text{Fe}_{82}\text{Si}_{6-x}\text{B}_9\text{P}_3\text{C}_x$ promotes an increase in the Fe element mass fraction from 92.94 wt.% for the C-0 alloy to 94.58 wt.% for the C-6 alloy, thereby elevating B_s . Secondly, the local environment plays a significant role in determining the ferromagnetic behavior within metallic glasses. Previous studies have reported that metalloids-sp/metal-d bonding leads to moment reduction in 3d-based amorphous alloys around 0 K, consequently causing a decrease in B_s . In terms of topology considerations, metalloids with smaller atomic radii possess lower theoretical coordination numbers [31], which diminishes metalloids-sp/metal-d bonding and subsequently increases the B_s value within amorphous alloys. Therefore, substituting Si with smaller atomic radius counterpart such as C tends to enhance the B_s value within an $\text{Fe}_{82}\text{Si}_{6-x}\text{B}_9\text{P}_3\text{C}_x$ alloy system. Combined with the observed variations in H_c and μ_e upon C addition, as

depicted in Table 2, it can be inferred that the soft magnetic properties can be effectively optimized through carbon incorporation. Notably, the C-2 alloy demonstrates exceptional comprehensive soft magnetic properties, characterized by a high B_s of 1.61 T, a low H_c of 1.7 A/m, and a significantly elevated μ_e reaching 10,608.

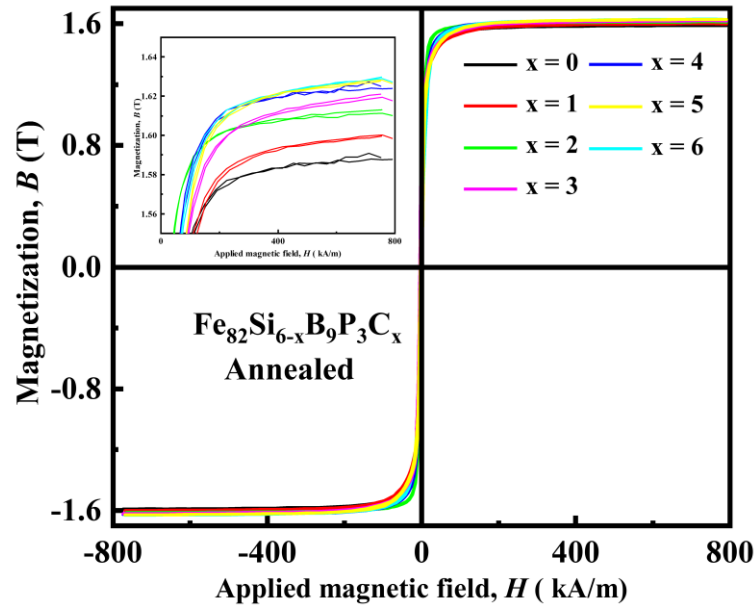


Figure 9. Hysteresis loops of the $\text{Fe}_{82}\text{Si}_{6-x}\text{B}_9\text{P}_3\text{C}_x$ amorphous alloys ribbons after annealing at suitable conditions.

Table 2. The relationship between B_s , H_c , and μ_e with varying C content.

Composition	B_s (T)	H_c (A/m)	μ_e (@1 kHz)
$\text{Fe}_{82}\text{Si}_6\text{B}_9\text{P}_3$	1.59	4.1	7800
$\text{Fe}_{82}\text{Si}_5\text{B}_9\text{P}_3\text{C}_1$	1.6	3.8	8134
$\text{Fe}_{82}\text{Si}_4\text{B}_9\text{P}_3\text{C}_2$	1.61	1.7	10608
$\text{Fe}_{82}\text{Si}_3\text{B}_9\text{P}_3\text{C}_3$	1.62	2.3	10108
$\text{Fe}_{82}\text{Si}_2\text{B}_9\text{P}_3\text{C}_4$	1.62	2.2	10333
$\text{Fe}_{82}\text{Si}_1\text{B}_9\text{P}_3\text{C}_5$	1.63	2.7	8046
$\text{Fe}_{82}\text{B}_9\text{P}_3\text{C}_6$	1.63	4.8	7163

To further investigate the reasons behind the changes in soft magnetic properties between C-0 and C-2 alloy ribbons in both as-spun and optimally annealed states, their magnetic domain patterns under zero field can be examined using a magneto-optical Kerr microscope, as depicted in Figure 10. It is evident from the figure that the magnetic structure of both alloys in the as-spun state exhibits irregularity, characterized by wide magnetic domains and numerous narrow domains. The rapid quenching process during fabrication induces significant internal stress in the as-spun ribbons, resulting in vertical magnetic anisotropy and a chaotic and irregular magnetic domain structure [32,33]. Internal stress, if present, can interact with the positive magnetostriction in the amorphous ribbons to induce a magnetic anisotropy perpendicular or parallel to the stress direction, depending on whether it is tensile or compressive in nature [34]. According to Tejedor et al.'s research [35], both surfaces of the as-spun amorphous ribbon experience compressive stress that gradually transitions into tensile stress at its center. Tsukahara et al. [36] observed that the magnitude of the anisotropy perpendicular to the stress determines the domain structure and width. Conversely, after annealing treatment, there is a transition in the easy magnetization direction accompanied by an increase in the domain width due to stress release [34,35]. As shown in Figure 10b,d, both C-0 and C-2 alloys exhibit wider magnetic

domain structures with relatively flat walls compared to their as-spun state counterparts. This uniformity facilitates the movement of the magnetic domains and the rotation of the magnetic moments during alloy magnetization process. Blázquez et al. [37] propose that, in Fe-based amorphous ribbons, there exists an inverse relationship between the coercivity and the width of magnetic domains, indicating that wider magnetic domains result in lower H_c values. Moreover, in comparison to the C-2 alloy, the C-0 alloy exhibits a certain degree of bifurcation in its magnetic domains with increased irregularity. This observation may be attributed to the fact that the C-2 alloy undergoes annealing at a temperature that is 20 °C higher than that of C-0 alloy; higher annealing temperatures are known to facilitate the unpinning process of magnetic domains. The analysis of domain patterns provides valuable insights into understanding the variations in H_c values for both C-0 and C-2 alloys under different conditions.

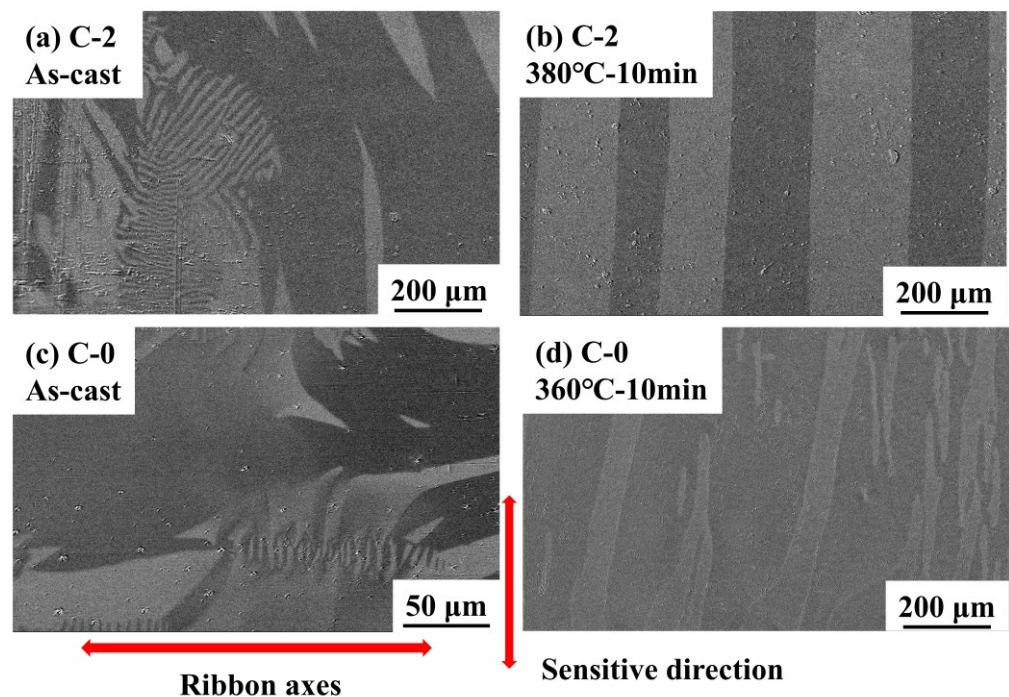


Figure 10. Images of magnetic domain structure of $\text{Fe}_{82}\text{Si}_{6-x}\text{B}_9\text{P}_3\text{C}_x$ ($x = 0, 2$) alloy ribbons under different states: (a) C-0 alloy, as-spun; (b) C-2 alloy, optimal annealing state; (c) C-0 alloy, as-spun state; and (d) C-2 alloy, optimal annealing state.

4. Conclusions

The effects of carbon addition on the amorphous FeSiBPC alloy systems were systematically investigated in this study, focusing on the AFA, thermal stability, and magnetic properties. The underlying mechanism responsible for the enhanced AFA and optimized soft magnetic properties was thoroughly analyzed and discussed. For as-spun $\text{Fe}_{82}\text{Si}_{6-x}\text{B}_9\text{P}_3\text{C}_x$ ($x = 0, 1, 2, 3, 4, 5,$ and 6) alloy ribbons prepared at a copper wheel velocity of 40 m/s, it was observed that alloys containing more than 1 atomic percent of carbon exhibited a fully amorphous structure. This suggests that incorporating an appropriate amount of carbon element can effectively enhance the AFA in this specific alloy system. The introduction of carbon to the C-2 and C-4 alloys resulted in higher E_{x1} and E_{p1} values compared to those observed in the C-0 alloy. This indicates that the proper incorporation of carbon enhances the thermal stability of these amorphous ribbons. Furthermore, the soft magnetic properties can be effectively optimized through the addition of C. By adding precisely 2 at. % C, the $\text{Fe}_{82}\text{Si}_4\text{B}_9\text{P}_3\text{C}_2$ alloy demonstrated optimized soft magnetic properties including a low H_c of 1.7 A/m, a high μ_e of 10608 ($f = 1$ kHz), and a relatively high B_s of 1.61 T. These improvements may be attributed to achieving a more homogeneous and optimized

magnetic domain structure through proper carbon addition. In conclusion, this work holds significant implications for the advancement of Fe-based soft magnetic amorphous alloys with high saturation magnetization.

Author Contributions: Conceptualization, F.L., R.W. and T.W.; methodology, W.Z. and T.W.; validation, S.W. and Y.C.; formal analysis, W.Z., C.C. and Y.C.; investigation, W.Z. and X.J.; resources, C.C. and S.W.; data curation, W.Z. and X.J.; writing—original draft preparation, W.Z.; writing—review and editing, R.W. and T.W.; supervision, F.L.; funding acquisition, T.W. and S.W. All authors have read and agreed to the published version of the manuscript.

Funding: This research was funded by the National Natural Science Foundation of China [Grant Nos. 52101203] and the Key Scientific Research Project of Colleges and Universities in Henan Province [Grant No. 24B430019].

Data Availability Statement: The raw data supporting the conclusions of this article will be made available by the authors on request.

Conflicts of Interest: The authors declare no conflicts of interest.

References

1. Silveyra, J.M.; Ferrara, E.; Huber, D.L.; Monson, T.C. Soft magnetic materials for a sustainable and electrified world. *Science* **2018**, *362*, eaao0195. [[CrossRef](#)] [[PubMed](#)]
2. Sharifikolouei, E.; Koziel, T.; Bała, P.; Żywczak, A.; Gondek, Ł.; Rashidi, R.; Fracasso, M.; Gerbaldo, R.; Ghigo, G.; Gozzelino, L.; et al. Cobalt-Based Metallic Glass Microfibers for Flexible Electromagnetic Shielding and Soft Magnetic Properties. *Adv. Electron. Mater.* **2024**, *10*, 2300490. [[CrossRef](#)]
3. Sharifikolouei, E.; Żywczak, A.; Sarac, B.; Koziel, T.; Rashidi, R.; Bala, P.; Fracasso, M.; Gerbaldo, R.; Ghigo, G.; Gozzelino, L.; et al. Soft Magnetic Properties and Electromagnetic Shielding Performance of Fe₄₀Ni₄₀B₂₀ Microfibers. *Adv. Electron. Mater.* **2023**, *9*, 2300178. [[CrossRef](#)]
4. Herzer, G. Modern soft magnets: Amorphous and nanocrystalline materials. *Acta Mater.* **2013**, *61*, 718–734. [[CrossRef](#)]
5. Gutfleisch, O.; Willard, M.A.; Brück, E.; Chen, C.H.; Sankar, S.G.; Liu, J.P. Magnetic Materials and Devices for the 21st Century: Stronger, Lighter, and More Energy Efficient. *Adv. Mater.* **2011**, *23*, 821–842. [[CrossRef](#)] [[PubMed](#)]
6. Jia, J.; Wu, Y.; Shi, L.; Wang, R.; Guo, W.; Bu, H.; Shao, Y.; Chen, N.; Yao, K. Influence of Annealing Process on Soft Magnetic Properties of Fe-B-C-Si-P Amorphous Alloys. *Materials* **2024**, *17*, 1447. [[CrossRef](#)] [[PubMed](#)]
7. Azuma, D.; Ito, N.; Ohta, M. Recent progress in Fe-based amorphous and nanocrystalline soft magnetic materials. *J. Magn. Magn. Mater.* **2020**, *501*, 166373. [[CrossRef](#)]
8. Li, X.; Zhou, J.; Shen, L.; Sun, B.; Bai, H.; Wang, W. Exceptionally High Saturation Magnetic Flux Density and Ultralow Coercivity via an Amorphous-Nanocrystalline Transitional Microstructure in an FeCo-Based Alloy. *Adv. Mater.* **2022**, *35*, e2205863. [[CrossRef](#)] [[PubMed](#)]
9. Shi, L.; Yao, K. Composition design for Fe-based soft magnetic amorphous and nanocrystalline alloys with high Fe content. *Mater. Des.* **2020**, *189*, 108511. [[CrossRef](#)]
10. Fan, Y.; Zhang, S.; Xu, X.; Miao, J.; Zhang, W.; Wang, T.; Chen, C.; Wei, R.; Li, F. Effect of the substitution of Si for B on thermal stability, magnetic properties and corrosion resistance in novel Fe-rich amorphous soft magnetic alloy. *Intermetallics* **2021**, *138*, 107306. [[CrossRef](#)]
11. Wang, T.; Chen, J.; Wei, R.; Chen, C.; Li, F. Improving the Bs and soft magnetic properties of Fe-based amorphous ribbons by manipulating the surface crystallization behavior. *J. Mater. Sci. Mater. Electron.* **2021**, *32*, 21206–21212. [[CrossRef](#)]
12. Ogawa, Y.; Naoe, M.; Yoshizawa, Y.; Hasegawa, R. Magnetic properties of high Bs Fe-based amorphous material. *J. Magn. Magn. Mater.* **2006**, *304*, e675–e677. [[CrossRef](#)]
13. Wang, A.; Zhao, C.; He, A.; Men, H.; Chang, C.; Wang, X. Composition design of high Bs Fe-based amorphous alloys with good amorphous-forming ability. *J. Alloys Compd.* **2016**, *656*, 729–734. [[CrossRef](#)]
14. Shi, L.; Qin, X.; Yao, K. Tailoring soft magnetic properties of Fe-based amorphous alloys through C addition. *Prog. Nat. Sci. Mater. Int.* **2020**, *30*, 208–212. [[CrossRef](#)]
15. Xu, J.; Yang, Y.Z.; Li, W.; Xie, Z.W.; Chen, X.C. Effect of the substitution of C for Si on microstructure, magnetic properties and bending ductility in high Fe content FeSiBCuPC alloy ribbons. *J. Alloys Compd.* **2017**, *727*, 610–615. [[CrossRef](#)]
16. Takenaka, K.; Setyawan, A.D.; Sharma, P.; Nishiyama, N.; Makino, A. Industrialization of nanocrystalline Fe–Si–B–P–Cu alloys for high magnetic flux density cores. *J. Magn. Magn. Mater.* **2016**, *401*, 479–483. [[CrossRef](#)]
17. Li, Y.L.; Dou, Z.X.; Chen, X.M.; Lv, K.; Li, F.S.; Hui, X.D. Improving the amorphous forming ability and magnetic properties of FeSiBPCu amorphous and nanocrystalline alloys by utilizing carbon. *J. Alloys Compd.* **2020**, *844*, 155767. [[CrossRef](#)]
18. Inoue, A. Stabilization of metallic supercooled liquid and bulk amorphous alloys. *Acta Mater.* **2000**, *48*, 279–306. [[CrossRef](#)]
19. Takeuchi, A.; Inoue, A. Classification of Bulk Metallic Glasses by Atomic Size Difference, Heat of Mixing and Period of Constituent Elements and Its Application to Characterization of the Main Alloying Element. *Mater. Trans.* **2005**, *46*, 2817–2829. [[CrossRef](#)]

20. Lopatina, E.; Soldatov, I.; Budinsky, V.; Marsilius, M.; Schultz, L.; Herzer, G.; Schäfer, R. Surface crystallization and magnetic properties of Fe_{84.3}Cu_{0.7}Si₄B₈P₃ soft magnetic ribbons. *Acta Mater.* **2015**, *96*, 10–17. [[CrossRef](#)]
21. Kong, F.L.; Chang, C.T.; Inoue, A.; Shalaan, E.; Al-Marzouki, F. Fe-based amorphous soft magnetic alloys with high saturation magnetization and good bending ductility. *J. Alloys Compd.* **2014**, *615*, 163–166. [[CrossRef](#)]
22. Zhao, C.; Wang, A.; He, A.; Yue, S.; Chang, C.; Wang, X.; Li, R.-W. Correlation between soft-magnetic properties and Tx1-Tc in high Bs FeCoSiBPC amorphous alloys. *J. Alloys Compd.* **2016**, *659*, 193–197. [[CrossRef](#)]
23. Peixoto, E.B.; Mendonça, E.C.; Mercena, S.G.; Jesus, A.C.B.; Barbosa, C.C.S.; Meneses, C.T.; Duque, J.G.S.; Silva, R.A.G. Study of the dynamic of crystallization of an amorphous Fe₄₀Ni₄₀P₁₄B₆ ribbon through Johnson-Mehl-Avrami model. *J. Alloys Compd.* **2018**, *731*, 1275–1279. [[CrossRef](#)]
24. Grishin, A.M.; Ignakhin, V.S.; Lugovskaya, L.A.; Osaulenko, R.N.; Sekirin, I.V. Crystallization kinetics and magnetostriction properties of amorphous Fe_{80-x}Co_xP₁₄B₆ metallic glasses. *J. Magn. Magn. Mater.* **2020**, *512*, 166972. [[CrossRef](#)]
25. Fan, X.D.; Shen, B.L. Crystallization behavior and magnetic properties in High Fe content FeBCSiCu alloy system. *J. Magn. Magn. Mater.* **2015**, *385*, 277–281. [[CrossRef](#)]
26. Zhu, L.; Jiang, S.S.; Yang, Z.Z.; Han, G.B.; Yan, S.S.; Wang, Y.G. Magnetic properties of a Fe-based amorphous alloy with stress gradient. *J. Magn. Magn. Mater.* **2021**, *519*, 167513. [[CrossRef](#)]
27. Shi, L.; Wang, K.; Yao, K. Maintaining high saturation magnetic flux density and reducing coercivity of Fe-based amorphous alloys by addition of Sn. *J. Non-Cryst. Solids* **2020**, *528*, 119710. [[CrossRef](#)]
28. Chazal, H.; Geoffroy, O.; Porteseil, J.L.; Waeckerlé, T. Influence of magnetoelastic effects on the coercivity of ultrasoft nanocrystalline alloys. *J. Magn. Magn. Mater.* **2004**, *272–276*, 1436–1438. [[CrossRef](#)]
29. Zhou, J.; Li, X.; Hou, X.; Ke, H.; Fan, X.; Luan, J.; Peng, H.; Zeng, Q.; Lou, H.; Wang, J.; et al. Ultrahigh Permeability at High Frequencies via A Magnetic-Heterogeneous Nanocrystallization Mechanism in an Iron-Based Amorphous Alloy. *Adv. Mater.* **2023**, *35*, 2304490. [[CrossRef](#)]
30. Xiao, H.; Dong, Y.; He, A.; Sun, H.; Wang, A.; Li, H.; Liu, L.; Liu, X.; Li, R. Magnetic softness and magnetization dynamics of FeSiBNbCu(P,Mo) nanocrystalline alloys with good high-frequency characterization. *J. Magn. Magn. Mater.* **2019**, *478*, 192–197. [[CrossRef](#)]
31. Miracle, D.B. Efficient local packing in metallic glasses. *J. Non-Cryst. Solids* **2004**, *342*, 89–96. [[CrossRef](#)]
32. Minoru, T.; Noritoshi, I.; Terunobu, M. The Variation of the Uniaxial Magnetic Anisotropy along the Thickness in an Amorphous Fe80P13C7 Alloy. *Jpn. J. Appl. Phys.* **1976**, *15*, 1821. [[CrossRef](#)]
33. Minoru, T.; Takao, S.; Terunobu, M. Magnetic Domains of an Amorphous Fe80P13C7 Alloy. *Jpn. J. Appl. Phys.* **1977**, *16*, 521. [[CrossRef](#)]
34. Gupta, P.; Akhila, K.J.; Srihari, V.; Svec, P.; Kane, S.R.; Rai, S.K.; Ganguli, T. On the origin of magnetic anisotropy of FeCo(Nb)B alloy thin films: A thermal annealing study. *J. Magn. Magn. Mater.* **2019**, *480*, 64–72. [[CrossRef](#)]
35. Tejedor, M.; Garcia, J.A.; Carrizo, J.; Elbaile, L. Mechanical determination of internal stresses in as-quenched magnetic amorphous metallic ribbons. *J. Mater. Sci.* **1997**, *32*, 2337–2340. [[CrossRef](#)]
36. Tsukahara, S.; Satoh, T.; Tsushima, T. Magnetic anisotropy distribution near the surface of amorphous ribbons. *IEEE Trans. Magn.* **1978**, *14*, 1022–1024. [[CrossRef](#)]
37. Blázquez, J.S.; Marcin, J.; Andrejka, F.; Franco, V.; Conde, A.; Skorvanek, I. Study of the Induced Anisotropy in Field Annealed Hitperm Alloys by Mössbauer Spectroscopy and Kerr Microscopy. *Metall. Mater. Trans. A* **2016**, *47*, 4301–4305. [[CrossRef](#)]

Disclaimer/Publisher’s Note: The statements, opinions and data contained in all publications are solely those of the individual author(s) and contributor(s) and not of MDPI and/or the editor(s). MDPI and/or the editor(s) disclaim responsibility for any injury to people or property resulting from any ideas, methods, instructions or products referred to in the content.